Editor's choice

Large-Scale Synthesis of Metal Additively-Manufactured Microstructures Using Markov Random Fields

Iman Javaheri [a,b,*], Mohsen Taheri Andani [c,d], Veera Sundararaghavan [b]

[a] NASA Langley Research Center, Hampton, VA, 23681, USA
[b] Department of Aerospace Engineering, University of Michigan, Ann Arbor, MI, 48109, USA
[c] Department of Mechanical Engineering, University of Michigan, Ann Arbor, MI, 48109, USA
[d] Department of Materials Science and Engineering, University of Michigan, Ann Arbor, MI, 48109, USA

ARTICLE INFO

ABSTRACT

A data-driven framework is developed and examined for creating spatially-varying crystallographic textures over component-scale Computer-Aided Design (CAD) models. Here, a set of three orthogonal 2D micrographs of an Additively-Manufactured (AM) specimen are first obtained experimentally through Electron Backscatter Diffraction (EBSD) and subsequently converted to a 3D representative unit cell using the Markov Random Field (MRF) technique. Features such as grain size, crystallographic orientation, and grain boundary misorientation distributions are used to validate the reconstructed 3D microstructure against input experimental EBSD images. The variations of microstructural features during a powder-based additive manufacturing process are subsequently modeled by merging patches from the 3D snapshot of AM microstructural unit cell in a part-scale geometry using a tensor-based optimization process. The optimization algorithm repeatedly pastes microstructural elements from the reconstructed MRF unit cell onto the geometrical CAD domain until it is entirely covered. Here, through a simple Graphical User Interface (GUI), the user specifies a tensor field over the volumetric CAD model, defining the local control over grain-scale, anisotropy, and crystal growth orientation. This new approach provides a workflow for reconstructing global maps of AM microstructures in real-time by embedding site-specific images based on known AM microstructural patterns seen in experimental characterization techniques. The numerical results are helpful specifically for the visualization of process–microstructure relationships in metal additive manufacturing techniques.

1. Introduction

With the emerging paradigm of Integrated Computational Materials Engineering (ICME) [1], multiscale design optimization approaches for tailoring engineering properties of Additively-Manufactured (AM) structures through controlled processing parameters [2–7] are of great interest to the design and additive manufacturing communities. Such multi-level simulations often involve solving process–microstructure-dependent properties to properly define the governing equations for macro-scale analyses. This requires models beyond the grain-scale level that can accurately capture the underlying morphology and texture of the materials [8,9]. The 2D microstructures are conventionally characterized through experimental instrumentations [10–13]. However, sectional information obtained from 2D empirical characterization techniques is generally insufficient for defining inherent microstructural parameters (e.g., neighbor connectivity, grain size/shape, boundary networks, etc.) [14,15]. Nevertheless, these parameters are a critical aspect of the materials design and can strongly affect the capability of

the structural systems to perform in their respective loading environments [16–18]. As a result, there has been a growing desire to develop accurate measurements, allowing for the direct acquisition of full-field 3D microstructural information [19,20].

The need to precisely characterize 3D microstructures has led to the development of several experimental methods, which are mainly variants of two major procedures: serial sectioning [21–23] and High-Energy Diffraction Microscopy (HEDM) [24–27]. Serial sectioning is a destructive approach in which layers of controlled thickness are sequentially polished away with high accuracy. This enables metallographic etching and captures sectional images of a material's microstructure. Post-processing follows to render these 2D images into a solid 3D model. Contrary to serial sectioning, HEDM is a non-destructive technique that uses high-energy X-rays to probe a relatively bulk specimen. The diffraction pattern in this approach determines the crystallographic orientations of the AM microstructure. Acquiring 3D

* Correspondence to: 2037 FXB Bldg, 1320 Beal Ave, Ann Arbor, MI 48109, United States.
E-mail addresses: imanajv@umich.edu (I. Javaheri), mtaheri@umich.edu (M.T. Andani), veeras@umich.edu (V. Sundararaghavan).

Nomenclature

Symbols in MRF sampling algorithm

S^i	Set of three orthogonal 2D exemplars taken along i-axis for $i = \{x, y, z\}$
$S^{i,w}$	Windows of size w (in pixel units) in corresponding S^i micrograph
$S_u^{i,w}$	RGB triplet of pixel u in respective $S^{i,w}$ window
V	Synthesized 3D microstructure
V_v	RGB triplet of voxel v in V
V_v^i	Spatial neighborhoods of voxel v along i-axis for $i = \{x, y, z\}$
$V_{v,u}^i$	RGB triplet of voxel u in respective cross-section V_v^i
S_v^i	Best-matching window to V_v^i in respective S^i exemplar
$S_{v,u}^i$	RGB triplet of pixel u in respective S_v^i window
$\omega_{v,u}^i$	Gaussian weighting factor associated with pixel u in respective $S^{i,w}$ window
$H(.)$	Histogram generator function for RGB channels

Symbols in LEGOMAT embedding algorithm

N	Total number of tetrahedra in each patch
T_0	Tetrahedral mesh seed
$v_1, \ldots, v_4$	Vertices of tetrahedral mesh seed T_0 in geometrical domain
$\Psi(v_1), \ldots, \Psi(v_4)$	Mapped vertices of $v_1, \ldots, v_4$, in the microstructural domain
$\tilde{P}, \tilde{Q}, \tilde{R}$	Local orthogonal vectors of tensor field within mesh seed T_0

Other symbols

θ, n	Angle-axis pair corresponding to crystal orientation
r	Rodrigues–Frank parameterization of crystal orientation
M	Orthonormal misorientation matrix
ϕ	Misorientation angle

microstructures with the above experimental techniques is generally a prodigious process and requires the aid of expensive empirical scanning devices. Additionally, such procedures uncover microstructural information over a relatively small volume of materials at a time. Hence, a large number of specimens must be scanned and seamlessly merged to generate a component-scale Computer-Aided Design (CAD) model. Such limitations reduce the general applicability of the experimental procedures, urging the development of robust computational reconstruction strategies [28,29].

Current numerical methods for predicting AM microstructure distributions are mainly physics-based techniques that require extensive computational efforts [7]. Amongst phase-field [30,31], kinetic Monte Carlo [32,33], and cellular automata [34,35] simulations, the phase-field modeling techniques are often considered the most accurate approaches that can adequately capture the solute concentration, precipitates, and dendrite shapes [36]. However, the advantage of using phase-field techniques is obscured by the required computational power, limiting the predictions to atomistic and continuum-length scales. Less costly than phase-field, cellular automata enables the scalability for larger domain sizes. However, the accuracy can diminish considerably

with increasing the cell size [37]. Additionally, the kinetic Monte Carlo simulations (e.g., SPPARKS) [32,38] allow large-scale predictions but have difficulties simulating the texture distributions and reconstructing complex components, such as non-equilibrium grain structures after the solidification process. To overcome such shortcomings, there has been considerable effort toward developing statistical-based models to generate representative microstructures. For instance, works based on feature-matching algorithms using correlation functions [39] or Markov Random Field (MRF) methods [40–43] can simulate microstructural components efficiently and are significantly less expensive compared to the aforementioned physics-based models.

Modern data-driven microstructure reconstruction methods such as MRF can employ snapshots of conventional 2D prototypes to rapidly generate diverse groups of microstructures for new processing modalities, such as hatch spacing, layer thickness, scan velocity, and effective laser energy density [28,43]. Consequently, here in this paper, an image-based framework based on the MRF reconstruction technique [43] is used for the real-time description of microstructure distribution of powder-based AM materials by combining material flow fields that capture microstructural variations in grain growth directionality, anisotropy, and grain sizes. Fundamental steps include: (*i*) experimental acquisition of orthogonal Electron Backscatter Diffraction (EBSD) scans of 2D microstructures, (*ii*) MRF for 3D reconstruction of the microstructural unit cell, and (*iii*) embedding the realized 3D microstructure into a virtual CAD geometry (i.e., a digital twin). As a result, the method builds global models based on locally-extracted images, warranting the term LEGOMAT: Locally-Extracted Globally-Organized Microstructural Models. The first version of LEGOMAT, as presented in this paper, is able to embed a single measured microstructure following the material flow path, while allowing the user to input parameters such as hatch spacing, layer thickness, and scan direction. Here, the algorithm reconstructs digital AM components, consisting of several laser passes and deposition layers, with microstructural information by mapping every finite element within the CAD model to a microstructural domain. The algorithm utilizes an iterative patch-based convergence criterion, minimizing the difference between the tensor fields associated with embedding microstructures to the specified local parameters in the CAD geometry. Such an approach can be used for a rapid reconstruction of 3D maps of microstructures with billions of grains at the component-scale level with user-defined processing modalities. Table 1 provides a comparison for the strengths and weaknesses of the LEGOMAT reconstruction approach against existing AM microstructure simulation techniques [7].

The following details the structure of the paper. The MRF algorithm for the reconstruction of 3D small-scale images from three 2D orthogonal EBSD exemplars is briefly described in Section 2.1. The LEGOMAT algorithm to embed the MRF synthesized microstructures is reviewed next in Section 2.2. Subsequently, the patch-based optimization process in correlation with material flow paths is described in detail. Thereafter, numerical and experimental results, along with statistical comparisons for verification of grain size, crystal orientation distribution, and grain boundary misorientation angles of the proposed methodology, are presented in Section 3. The efficacy (i.e., computational cost and accuracy) of the LEGOMAT reconstruction framework is then compared against known experimental characterization patterns and simulated images from SPPARKS kinetic Monte Carlo [32].

2. Methodology

In this section, the mathematical formulation and implementation for reconstructing large-scale 3D AM microstructures are discussed. The overall process, as illustrated in Fig. 1, utilizes two separate algorithms. First outlined in Section 2.1, the MRF theory, from a previously-published work by authors [43], is summarized. There, the 2D microscopy imaging along with the MRF sampling algorithm is leveraged to reconstruct a representative 3D microstructural unit cell from three

Table 1

Comparison of computational methods for microstructure predictions in metal additive manufacturing.

Method	Computational cost	Benefits	Challenges
Phase-field	Extremely high	Simulates both solidifications and solid-state phase transformations	Is not suitable for large-scale predictions
Cellular automata	High/intermediate (depending on spatial domain being constructed)	Simulates solid-state transformations, and enables crystallographic texture predictions	Accuracy of microstructure simulations depends on cell size
Kinetic Monte Carlo	Intermediate	Allows for large-scale domains (dozens of layers and passes)	Unable to predict crystallographic texture, and neglects effect of temperature accumulation on melt pool geometry
LEGOMAT	Low	Allows for large-scale domains (dozens of layers and passes), and crystallographic texture predictions	Requires microstructural libraries and knowledge of grain growth directions

orthogonal planar experimental EBSD exemplars. Next, Section 2.2 describes the LEGOMAT large-scale synthesis process for embedding site-specific unit cells through a tensor-based optimization procedure that efficiently merges patches from the 3D unit cell onto a CAD model.

2.1. Generation of 3D unit cells - MRF sampling algorithm

The input to the MRF algorithm consists of three orthogonal planar EBSD exemplars of an AM microstructure, whereas the output is a statistically-equivalent 3D solid model of the same microstructure. The overall process closely follows the numerical procedure published in Javaheri et al. [43]. The key ingredients of the process are described briefly here. Let S^i for $i = \{x, y, z\}$ denote a set of three orthogonal experimentally-obtained slices of an AM microstructure along the respective x, y, and z directions. The symbol V indicates the synthesized

3D microstructure, with V_v representing the Red–Green–Blue (RGB) coloring of the voxel v. In the realm of microstructures, RGB channels (as a triplet) are often used for the representation of the phase information (e.g., crystal orientations, chemical compositions, etc.). Based on the Markovian assumption, the Probability Density Function (PDF) of a voxel given the states of its spatial neighborhood is independent of the entire dataset. Thus, only neighbors over a relatively small window around the voxel v are examined throughout the sampling process. As seen in Fig. 2(a), the vector denoting the spatial neighborhood of voxel v in the slice orthogonal to the i-axis is denoted as V_v^i, where $i = \{x, y, z\}$. Additionally, let $S^{i,w}$ denote a window of the same size in its respective 2D micrograph S^i. Using the Markovian properties, the most likely RGB triplet of the voxel v can thus be estimated by identifying center pixel values of $S^{i,w}$ in the planar micrographs that
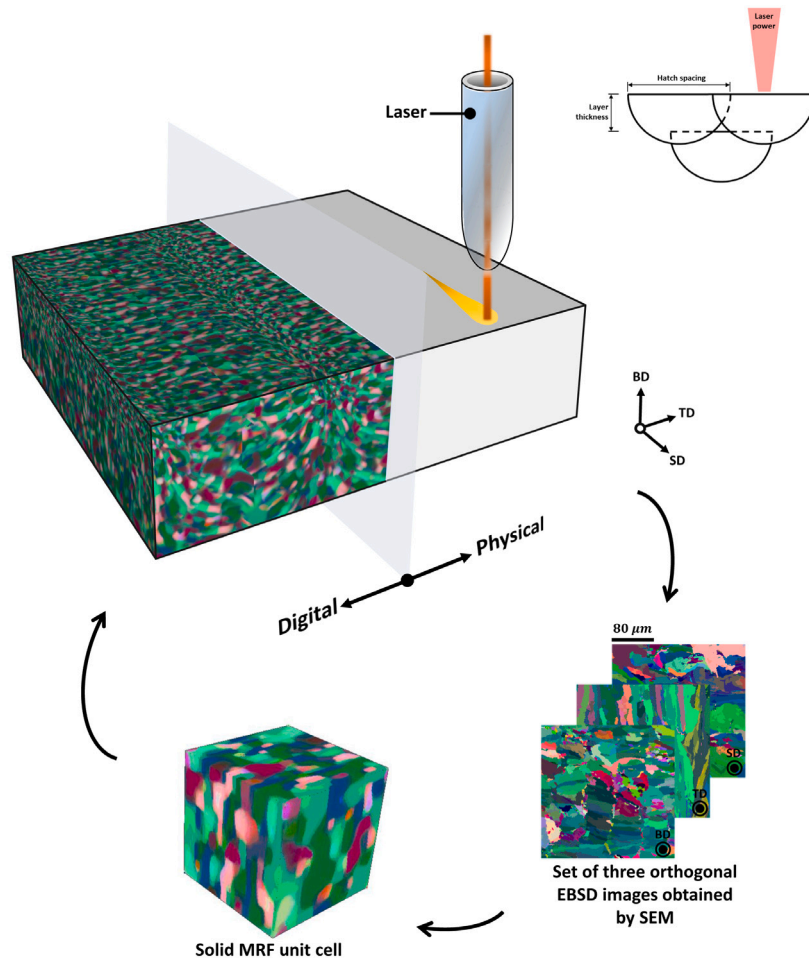

Fig. 1. LEGOMAT approach: full-field component imaging built by using a single site-specific MRF unit cell. Here, a small-scale texture of the AM 316L stainless steel specimen in three orthogonal planes is first extracted through Scanning Electron Microscopy (SEM) imaging. The 3D microstructure is then reconstructed using the MRF sampling algorithm as introduced in Javaheri et al. [43]. The laser path, along with other processing parameters such as layer thickness and hatch spacing (imposed by the user), are then used to embed the crystallographic patches from the MRF unit cell onto the CAD model. The *BD*, *SD*, and *TD* axes here represent the *Building*, *Scanning*, and *Transverse Directions*, respectively.

best resemble the corresponding cross-sections of $\boldsymbol{V}_v^i$. These windows, as shown in Fig. 2(b), are denoted by $\boldsymbol{S}_v^i$, where $i = \{x, y, z\}$.

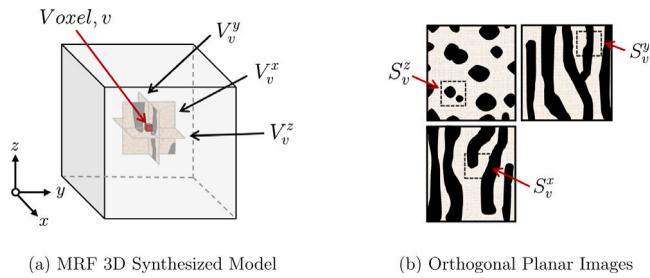(a) MRF 3D Synthesized Model   (b) Orthogonal Planar Images

Fig. 2. MRF unit cell reconstruction schematic: (a) the neighborhoods of the voxel v in the slices orthogonal to the $i = \{x, y, z\}$ axes, denoted as $\boldsymbol{V}_v^i$, are shown. (b) The windows in the input 2D micrographs shown in dotted lines are denoted by $\boldsymbol{S}_v^i$. These windows closely resemble the neighborhoods of the orthogonal cross-sections of voxel v, $\boldsymbol{V}_v^i$.

Subsequently, let the value $\boldsymbol{V}_{v,u}^i$ denote the RGB coloring of voxel u in the neighborhood of $\boldsymbol{V}_v^i$. Let the values $\boldsymbol{S}_{v,u}^i$ and $\boldsymbol{S}_u^{i,w}$, respectively denote the RGB triplets of pixel u in the windows $\boldsymbol{S}_v^i$ and $\boldsymbol{S}^{i,w}$. Consequently, the best-matching neighborhood of voxel v, $\boldsymbol{S}_v^i$, in each orthogonal planer image is selected by solving the following minimization problem:

$$\boldsymbol{S}_v^i = \arg \min_{\boldsymbol{S}^{i,w}} \sum_u \omega_{v,u}^i \|\boldsymbol{V}_{v,u}^i - \boldsymbol{S}_u^{i,w}\|_2^2 \tag{1}$$

where $\|\cdot\|_2$ represents the L_2 norm, and $\omega_{v,u}^i$ denotes a per-pixel radially-symmetric weighting factor, preserving the short-range correlations of the nearby pixels/voxels. Here, a Gaussian distribution-based function [43] is used to drive the corresponding influence weighting factors, such that the magnitudes of the weights for nearby pixels/voxels are taken to be larger than the ones farther away.

The process outlined in Eq. (1) consists of an exhaustive search that compares all the windows in the input 2D exemplars, $\boldsymbol{S}^{i,w}$, to the corresponding neighborhood of voxel v, $\boldsymbol{V}_v^i$, and identifies windows, $\boldsymbol{S}_v^i$, that lead to a minimum weighted squared Euclidean distance. Generally, the center pixel values in $\boldsymbol{S}_v^i$ for $i = \{x, y, z\}$ are composed of distinct RGB triplets. Yet, an optimal value of $\boldsymbol{V}_v$ needs to be inferred by weighting colors pertaining to location v not only in the matching windows of voxel v but also in its surroundings as follows:

$$\boldsymbol{V}_v = \left(\sum_{i \in \{x,y,z\}} \sum_u \omega_{u,v}^i \boldsymbol{S}_{u,v}^i \right) / \left(\sum_{i \in \{x,y,z\}} \sum_u \omega_{u,v}^i \right) \tag{2}$$

note that the subscripts u and v are switched in Eq. (2), compared to Eq. (1). This implies that the optimal color of the voxel v, $\boldsymbol{V}_v$, is the weighted-average of the colors at locations corresponding to voxel v in the best-matching windows of voxels u found within the synthesized 3D microstructure. The RGB channels here are averaged independently. Since $\boldsymbol{V}_v$ is continuously changing after each step, the set of closest input neighborhoods $\boldsymbol{S}_v^i$ may vary accordingly after each iteration. Hence, the above two steps are repeated until convergence; that is, until the set of $\boldsymbol{S}_v^i$ remains unchanged.

Furthermore, the color space associated with micrographs is typically discrete and range-bound. Consequently, the averaging performed in Eq. (2) always tends to shrink the color levels. For instance, the color level 0 has the tendency to increase, due to it being averaged with all the color levels that are greater or equal to 0. However, the assumption in MRF reconstruction remains that the two datasets (i.e., three orthogonal planar exemplars and the solid synthesized model) have the same Cumulative Distribution Function (CDF) of color densities. As a result, given the reference exemplars and the target synthesized images, the MRF algorithm normalizes the color histograms at the end of each iteration by first binning the colors into 255 discrete intervals.

Thereafter, histogram matching, as demonstrated in Fig. 3, is applied independently for each RGB color channel such that the color density of the synthesized model closely matches with the planar exemplars [43].
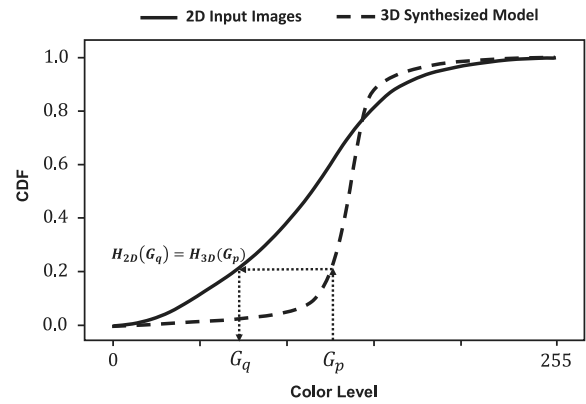

Fig. 3. Histogram matching algorithm: given the reference (2D) and the target (3D) images, the color histograms are obtained by binning the colors into 255 discrete intervals. Cumulative Distribution Functions (CDFs) of the two color histograms, denoted as $H_{2D}(.)$ and $H_{3D}(.)$, are then computed and normalized. The color level G_p in the synthesized 3D image is adjusted for each RGB channel independently. The new color G_q has the same CDF as in input 2D exemplars.

Although the methodology presented here is not tied to any specific image resolution, all the input exemplars are initially re-sampled to 128×128 pixels prior to the 3D reconstruction. Next, a random RGB triplet from the input planar exemplars is assigned to each voxel v, as an initial condition. The MRF reconstruction process is then carried out in a multi-resolution framework: starting with a coarse voxelated mesh while progressively interpolating the results to a finer resolution. The multi-resolution approach considerably increases the convergence rate associated with the sampling algorithm. As such, three resolution levels 32^3, 64^3, and 128^3 are sequentially used for presented MRF unit cell reconstructed examples. The computational cost for generating the MRF unit cell is directly related to the pixel resolution and the sampling window size. In the unit cell reconstruction framework, the majority of the computational burden is related to identifying the best-matching expectations in the orthogonal input images. The detailed computational breakdown can be found in [43]. In the following section, the numerical process associated with the LEGOMAT for embedding the location-specific unit cell in an engineering-scale geometry is discussed.

2.2. Large-scale synthesis - LEGOMAT embedding algorithm

The inputs of the LEGOMAT algorithm consist of a geometrical CAD model and an exemplar solid 3D unit cell of an AM microstructure, as outputted from the MRF reconstruction process. Here, the input CAD geometry is discretized into tetrahedral meshes via Delaunay tetrahedralization algorithm [44]. In return, the LEGOMAT output is of a 3D CAD model filled with microstructural patches from the exemplar 3D unit cell. It is worth noting that the LEGOMAT algorithm, as presented in this paper, is a stand-alone approach and can be ultimately utilized to reconstruct a wide range of part-scale 3D solid textures using input unit cells obtained from either experimental procedures or other existing numerical techniques (e.g., DREAM.3D, Neper, etc.). The MRF algorithm, however, is notably more suitable for reconstructing small-scale AM unit cells since it can systematically model realistic grain structures (e.g., non-convex and non-equilibrium grain structures) without assuming an idealized morphology based on Voronoi tessellation employed in Neper [45] or superellipsoid geometrical approach in DREAM.3D [46]. Furthermore, the generation of statistically-representative 3D numerical models via DREAM.3D or Neper generally requires information such as spatial distributions and 3D grain shapes, which is not readily attainable from a limited set of orthogonal planar exemplars as used in this paper.

Metal additive manufacturing processes can often be classified based on powder-delivery methods into two general categories: Laser Engineered Net Shaping (LENS) and Laser Powder-Bed Fusion (LPBF). The LENS process utilizes a carrier gas stream to transport powder through a nozzle directly onto the melt pool at the surface of the build. In LPBF, however, a laser beam often rasters across the metallic powder bed. Although these two manufacturing techniques have markedly different melting and solidification dynamics, they often exhibit similar underlying microstructural patterns. In particular, the solidification process results in the formation of highly-localized non-equilibrium microstructural components within the fusion zone [47–49]. Preferred crystallographic growth directions in these manufacturing techniques tend to align the columnar grains in the direction of increasing temperature. For instance, on the *SD* plane, the columnar grains tend to grow perpendicular to the melt pool's solidification surface, while curving toward the laser beam directions [50,51]. Hence, the alignment of such complex features in 3D geometrical space while using a single reference 3D snapshot, requires a tensor field (i.e., a set of three orthogonal vector fields) that can thoroughly capture the underlying material growth orientations after the solidification process.

In the current implementation, as illustrated in Fig. 4(b), a volumetric vector field is specified over the CAD model, simply by manually drawing the material growth directions on the surface and cross-sections of the CAD model. The second direction of the tensor field is then chosen randomly upon embedding each microstructural element, and the third direction is set to be the cross-product of the two vectors. Alternatively, the volumetric tensor field can be automatically inferred directly by the experimental measurements. However, such measurements are only possible to obtain on external surfaces of the build and not at the interior locations. Though, one can incorporate Computational Fluid Dynamics (CFD) simulations to reproduce the volumetric

temperature gradient that can ultimately inform the preferred material flow directions [52,53]. The latter approach is outside the scope of the presented methodology. However, it will be incorporated in future studies upon automation of the material growth directions based on a set of input parameters such as hatch spacing, layer thicknesses, and scanning patterns. For interpolation of the user-specified vectors, a Laplacian smoothing [54] is utilized, which has been previously employed in lapped texture synthesis methods [55,56]. Once the material flow paths are scribed, the local scaling of the grain sizes, as seen in Fig. 4(c), is specified to incorporate size-varying crystals in the CAD model. Additional details regarding the manual specification of material flow fields and grain size scaling are provided in Sections Sections 2.2.1 and 2.2.2, respectively. Next, the LEGOMAT algorithm, as outlined in Section 2.2.3, repeatedly pastes the microstructural patches from the MRF unit cell onto the CAD model while aligning the embedding microstructures according to the local tensor orientation and specified scaling parameter. The result of the embedding process is shown in Fig. 4(d) along with a few of its cross-sections across each orthogonal direction.

Contrary to the voxelated filling approach outlined in Section 2.1, a patch-based optimization technique is implemented here that uses a tetrahedral discretization to represent the solid geometrical CAD models. This formulation has certain benefits over voxel representation used in Section 2.1. The main advantage is it requires a substantially smaller number of elements to approximate the 3D CAD model, resulting in considerably fewer iterations (and equivalently lower computational cost) to complete its reconstruction task. Next, the manual specifications of the material flow field, grain size scaling, along with numerical embedding process and its implementation are explained in detail in Sections 2.2.1–2.2.3.
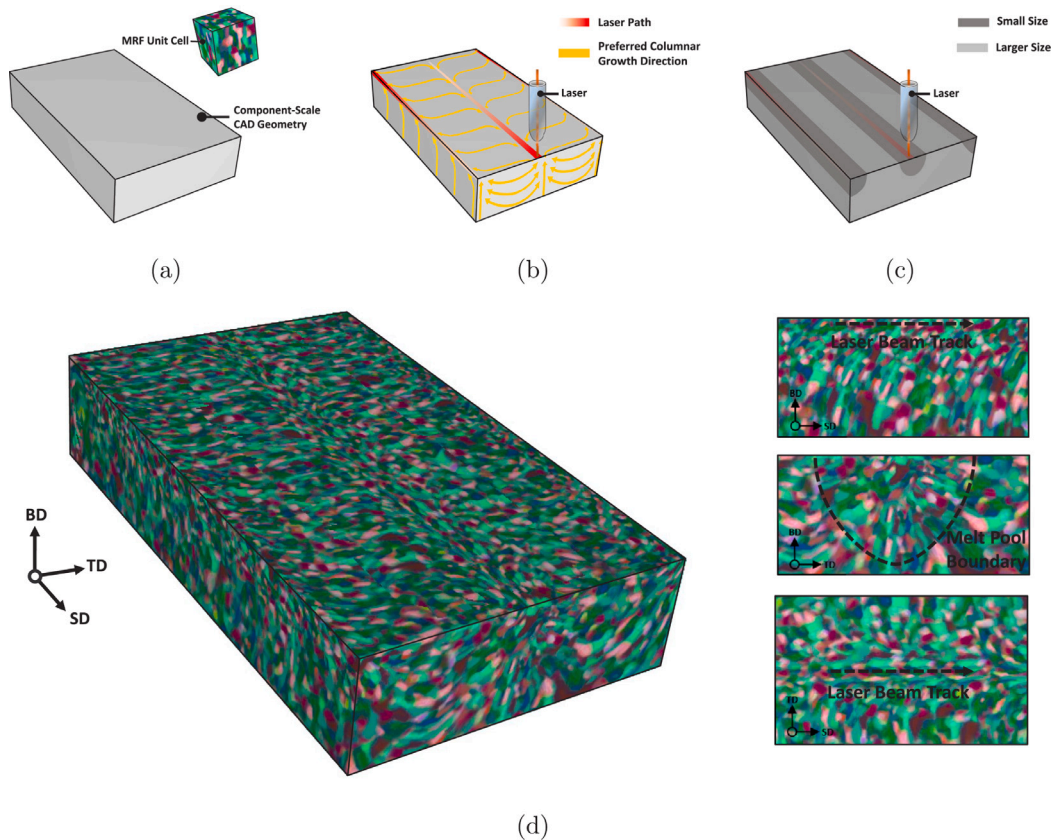

(a)   (b)   (c)

(d)

Fig. 4. Illustration of LEGOMAT embedding process: (a) inputting the geometrical mesh along with 3D solid microstructural unit cell, (b) manually drawing the local vector fields, representing the preferred crystallographic growth orientation, (c) setting up the grain-scale parameterization by embedding larger grains farther away from the laser path, (d) result of LEGOMAT's embedding procedure, along with snapshots of three orthogonal cross-sections in the realized CAD structure.

2.2.1. Material flow fields

In this paper, the preferred crystallographic growth orientations illustrated in Fig. 4(b) are manually drawn as a set of orthogonal vector fields based on known microstructural patterns seen in experimental characterization techniques. Upon specification of the growth orientations, the LEGOMAT optimization procedure in Section 2.2.3 closely follows the local directional vector fields throughout the embedding process of the microstructural patches from the MRF unit cell onto the CAD model. In structural systems manufactured by LENS or LPBF techniques with a zig-zag rastering pattern, columnar-shape-like grains are formed away from the laser beam track along the BD surface in-plane to the build. Additionally, on the SD plane, columnar grains tend to elongate perpendicular to the melt pool's solidification boundary while curving in the direction of increasing temperature (i.e., toward laser beam track) [5,16,23,35]. On the TD surface, the elongated grains tend to extend nearly perpendicular to the laser beam track while becoming slightly inclined toward SD at regions closer to the beam track [5,23,38,48,57,58]. Accordingly, given an input CAD model and processing modalities, the user can follow the above crystallographic growth patterns by manually drawing the columnar directions across surfaces orthogonal to the laser direction. The second direction of the tensor field is then chosen at random upon embedding each microstructural element. At the same time, the third direction is set to be the cross-product of the two local vector fields. For volumetric interpolation of these vectors, a Laplacian smoothing scheme [54] is employed to approximate the preferred growth directions across non-trivial faces with unspecified or unknown growth directions. The process for the manual drawing of the first directional vector pertaining to the crystal growth direction along with relative experimental images from the work of Rodgers et al. [32] for a LENS build with a zig-zag rastering pattern is shown in Fig. 5.

2.2.2. Material grain size

As evident from experimental characterization techniques of AM components [5,32,38,48,58], small grains near the laser path tend to nucleate during the solidification process. These grains, however, quickly transition to much larger elongated grains in between the laser paths. Such transitions often result in three classes of grain morphology depending on location within the build: (i) large curved columnar grains on TD and SD planes, (ii) fine equiaxed grains near the laser

path on BD plane, and (iii) large transversely-elongated columnar grains across regions in between the laser paths across BD surface. The resulting heterogeneous mixture of elongated and equiaxed grains often has a visible periodicity with the deposition thickness, hatch spacing, and scanning pattern [32]. This transition is further controlled by the thermal gradient and solidification rate at the solid–liquid interface. For instance, the width corresponding to small-scale grains along the laser beam track often tends to grow with increasing laser speed or decreasing laser power [58]. Fig. 6 illustrates these grain types in cross-sectional regions orthogonal to the scan direction. Although the curvature of these grains is mainly controlled by the directional vector fields outlined in Section 2.2.1, for a more realistic reconstruction, grain-scale parameterization must also be specified before initiating the embedding process in Section 2.2.3. Accordingly, in the LEGOMAT approach, the user may enforce smaller grain scales near the laser path in cross-sections perpendicular to the scan direction. Such an approach can efficiently create the equiaxed-to-columnar grain transition, as elaborated above. The process for the manual specification of the grain size parameterization for an AM build with a zig-zag tracing pattern is shown in Fig. 6.

2.2.3. Tensor-based optimization procedure

The LEGOMAT embedding process closely follows the lapped texture reconstruction technique outlined in the work of Praun et al. [56], which was initially developed for 2D texture embedding. Here, in the process of volumetric embedding, a group (or a *patch*) of N tetrahedral elements, denoted as T_i for $i = 0, 1, 2, \ldots, N - 1$, is selected in the CAD model such that there are slight variations in the user-defined tensor field across the group. The size of the group of tetrahedral elements is always chosen to be contained within the representative input MRF microstructure. In particular, let the tetrahedron located at the center of the patch, denoted by T_0, constitute as the seeding element. The LEGOMAT algorithm then acquires all neighboring elements of the seed tetrahedron for which the following two conditions are satisfied: (i) the mapped vertices of the tetrahedron T_i are inside the microstructural unit cell, and (ii) the dot product between the tensor fields associated with seed tetrahedron T_0 and the element T_i is greater than zero. In the case of uniform discretization, the total number of assigned elements at each iteration varies considerably based on global processing modalities and relative spatial locations to the laser path. Generally, fewer elements are assigned along the laser path, where grain size scaling
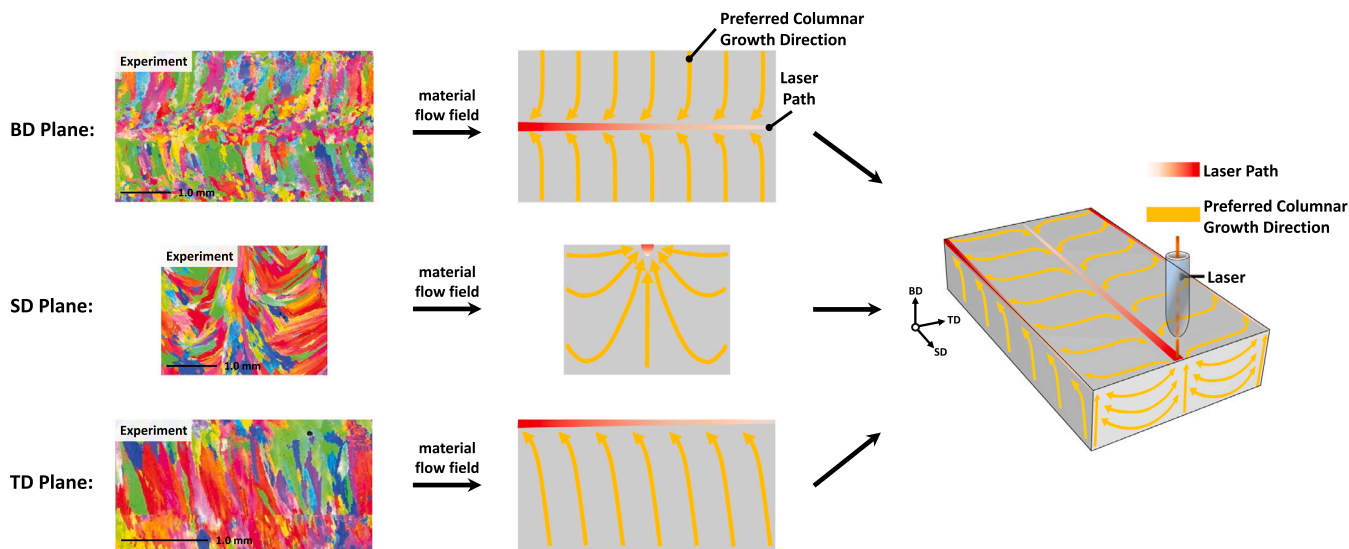

Fig. 5. Manual drawing of local vector fields, representing the preferred crystallographic growth orientation, based on known microstructural patterns seen from the experimental characterization techniques. The shown *TD* image is taken from the centerline of a beam pass. The experimental images are reproduced from the work of Rodgers et al. [32] under the terms of the Creative Commons CC-BY license.
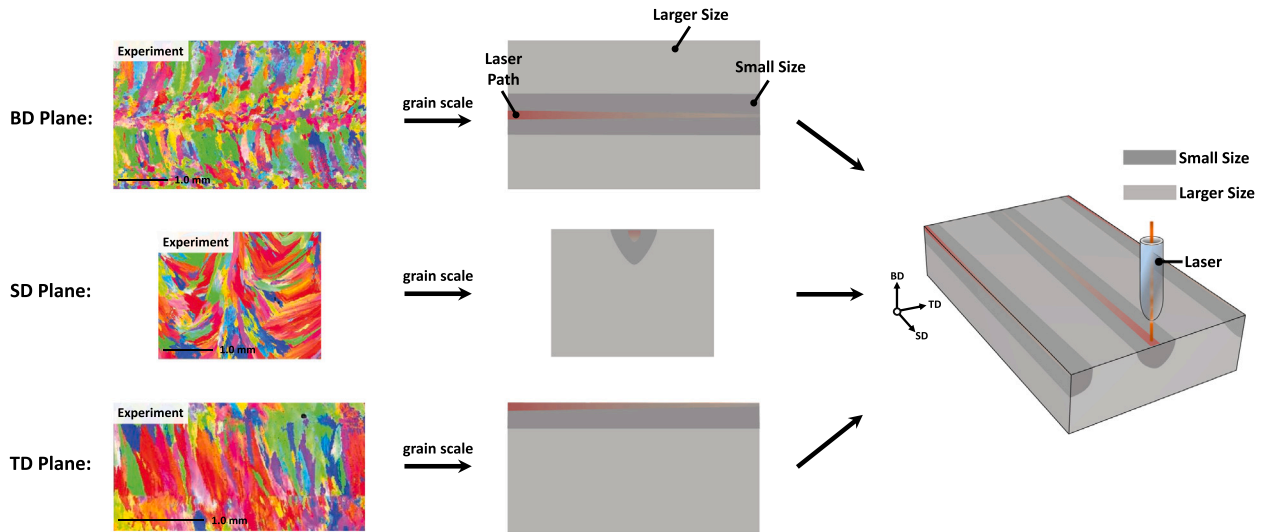
Fig. 6. Manual parameterization of grain size scaling by embedding larger grains farther away from the laser path in cross-sections orthogonal to the scan direction. The experimental images shown here are reproduced from the work of Rodgers et al. [32] under the terms of the Creative Commons CC-BY license.

is small. In contrast, more significant numbers of tetrahedra are being filled simultaneously at locations closer to the melt pools boundary.

The embedding algorithm is based on an optimization process that computes the mapping of the vertices of the 4-node tetrahedral elements T_i within each patch, to locations in the MRF microstructure that closely resemble the user-specified tensor field. In the following discussion, let $v_1, \ldots, v_4$ represent four vertices of the seed tetrahedron T_0 in the CAD model. Accordingly, the primary aim of the LEGOMAT embedding process is to identify the linear mapping of these nodes to positions $\Psi(v_1), \ldots, \Psi(v_4)$ in the representative MRF unit cell.

Here, let $\tilde{P}$, $\tilde{Q}$, and $\tilde{R}$ represent the set of three local orthogonal vectors of the tensor field associated with the seed tetrahedron, T_0. Consequently, the barycentric coordinates, denoted as $p_1, \ldots, p_4$, of tetrahedral element T_0 can be used to represent $\tilde{P}$ as follows:

$$\begin{cases} p_1 v_1 + p_2 v_2 + p_3 v_3 + p_4 v_4 = \tilde{P} \\ p_1 + p_2 + p_3 + p_4 = 0 \end{cases} \tag{3}$$

Similarly, $\tilde{Q}$ and $\tilde{R}$ can be represented using $q_1, \ldots, q_4$ and $r_1, \ldots, r_4$, respectively. Furthermore, due to the mapping associated with vertices, i.e., $v_j \mapsto \Psi(v_j)$ for $j = \{1, 2, 3, 4\}$, being linear, the mapping of vector $\tilde{P}$ in the CAD model to the corresponding vector $\Psi(\tilde{P})$ in the microstructural space follows the same weighting factors as in Eq. (3), as formulated below:

$$\Psi(\tilde{P}) = p_1 \Psi(v_1) + p_2 \Psi(v_2) + p_3 \Psi(v_3) + p_4 \Psi(v_4) \tag{4}$$

Similarly, $\Psi(\tilde{Q})$ and $\Psi(\tilde{R})$ can be formulated in terms of barycentric coordinates $q_1, \ldots, q_4$ and $r_1, \ldots, r_4$, respectively. Ideally, when mapped onto the microstructural domain, these vectors should be aligned with the orthogonal x, y, and z coordinate axes in the microstructure. However, as illustrated in Fig. 7, slight differences are permitted in order to enforce microstructural continuity in the CAD model. Therefore, difference vectors, denoted as d_p, d_q, and d_r, are defined for the seed tetrahedron, T_0, as follows:

$$\begin{cases} d_p = \Psi(\tilde{P}) - (1, 0, 0)^t \\ d_q = \Psi(\tilde{Q}) - (0, 1, 0)^t \\ d_r = \Psi(\tilde{R}) - (0, 0, 1)^t \end{cases} \tag{5}$$

Similarly, the difference vectors associated with all tetrahedral elements in the patch, i.e., T_i for $i = 0, 1, 2, \ldots, N - 1$, can be computed.

Therefore, let d_p^i, d_q^i, and d_r^i denote the difference vectors associated with the tetrahedral element T_i. The LEGOMAT optimization problem is to find the vertex mapping for all 4-node tetrahedra T_i within the patch such that the least-squares functional defined below is minimized:

$$\mathcal{F} = \frac{1}{N} \sum_{i=0}^{N-1} \|d_p^i\|_2^2 + \|d_q^i\|_2^2 + \|d_r^i\|_2^2 \tag{6}$$

However, the minima corresponding to Eq. (6) is unique up to a translation vector. Thus, an additional constraint, as formulated below, is set to fix the center of the seed tetrahedron, T_0, to the center of the microstructural volume:

$$\frac{\Psi(v_1) + \Psi(v_2) + \Psi(v_3) + \Psi(v_4)}{4} = (0.5, 0.5, 0.5)^t \tag{7}$$

Consequently, the optimized solution for mapped vertices associated with T_i for $i = 0, 1, 2, \ldots, N - 1$ from the constrained minimization problem formulated in Eqs. (6)–(7), can be efficiently obtained by solving a sparse linear system of equations. Once the patch of tetrahedral elements T_i is fully mapped to the microstructural space, the LEGOMAT optimization procedure randomly continues with another location in the CAD model consisting of an unmapped tetrahedron. The embedding process repeats until all the nodes in the CAD model are mapped to the microstructural unit cell.

The tensor-based optimization procedure elaborated here is specific to a 4-node tetrahedral discretization. Generally, partitioned elements need to allow for a linear interpolation of coordinates or variables as formulated in Eqs. (3)–(4). Accordingly, a 10-node tetrahedron will have non-linear interpolants and so need further modifications in the LEGOMAT optimization algorithm to implement the mapping process of the tensor fields in the CAD model onto the MRF microstructure. The LEGOMAT algorithm and its Graphical User Interface (GUI) for the manual drawing of material growth direction and grain size scaling are implemented using *C++* and *OpenGL*. Furthermore, large-scale microstructure simulation times generally vary drastically depending on the complexity of material flow fields (e.g., number of paths, layers, etc.) and the mesh density in the CAD model. Amongst all the steps described in Section 2.2, the manual drawing of the volumetric vector field is the most time-consuming process, especially for multi-layer, multi-track scenarios. Nonetheless, LEGOMAT reconstruction framework is still fairly inexpensive in terms of computation and memory for representing large-scale solid models.
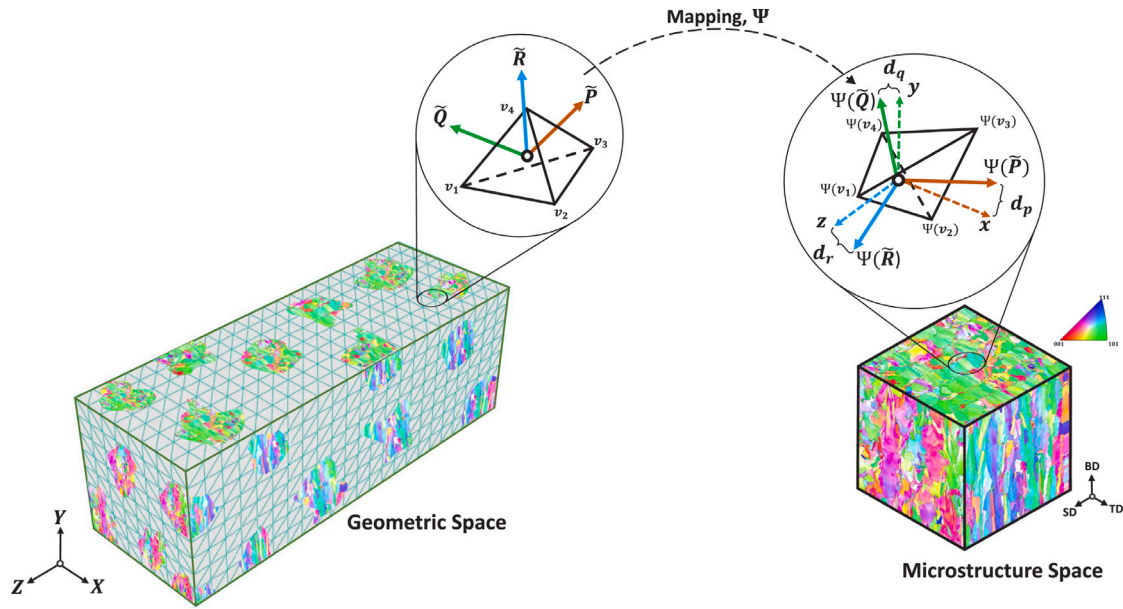
Fig. 7. LEGOMAT optimization schematic: the optimization process minimizes the difference vectors d_p, d_q, and d_r between microstructure coordinate axes x, y, z and respective transformed axes $\Psi(\widetilde{P})$, $\Psi(\widetilde{Q})$, $\Psi(\widetilde{R})$ for each tetrahedron.

3. Results and discussion

In this section, the process parameters for manufacturing and image acquisition of EBSD sections of the AM 316L stainless steel specimen are explained. Thereafter, the results for reconstructing digital twins using a set of locally orthogonal planar images are highlighted. The efficacy of the MRF algorithm is assessed by comparing the crystallographic orientations, grain boundary misorientations, and grain size statistics of the synthetic and experimental images. Next, the LEGOMAT algorithm is used for the simulation of various part-scale AM microstructures consisting of multi-layer and multi-track processes. The part-scale results are then compared against known experimental imaging and simulated microstructures using SPPARKS kinetic Monte Carlo simulator [32].

The 316L stainless steel specimen was fabricated via a Selective Laser Melting (SLM) 280 HL machine, equipped with two 400 W Continuous Wave (CW) Ytterbium fiber laser beams with approximately 80 μm diameter at the focal point. The SLM 280 HL machine is composed of a building platform with a maximum capacity of $280 \times 280 \times 350$ mm^3. Prior to the operation, argon gas was flooded into the chamber to lower the oxygen level below 0.1%. The pre-alloyed 316L stainless steel powder, with particle sizes between $30 - 50$ μm, was used as the printing substance. A fully-dense cuboid of $10 \times 6 \times 10$ mm^3 sample was fabricated for microscopic analysis using the manufacturer recommended guidelines with core processing parameters of 200 W laser power, 800 mm/s scan speed, 30 μm layer thickness, and 120 μm hatch spacing. The AM volume was printed using a bi-directional scanning technique at which the laser beam moved across each layer in a zig-zag pattern. The cuboidal sample was then sequentially polished through diamond suspensions of 9 μm, 6 μm, and 3 μm. This followed by alumina suspensions of 1 μm and 0.05 μm, intending to achieve fine smooth faces. The EBSD analyses of three orthogonal 700×700 μm^2 faces of the cuboidal specimen were subsequently performed using a high-resolution Scanning Electron Microscopy (SEM) TESCAN MIRA3, equipped with an EDAX Hikari XP EBSD detector. These orthogonal sections were mounted separately using a slow-set epoxy. Each EBSD scan was taken at 30 kV voltage and 1.0 μm step size. The EBSD camera parameters were set to 1×1 binning, high-gain, and low-exposure to achieve an average Confidence Index (CI) of 0.6.

Once the experimental EBSD images were generated, the raw Euler angles were mapped to nodes in a discretized Orientation Distribution

Function (ODF). The ODF provides a probability density of the crystallographic textures by describing the Euler angles associated with each node in the Rodrigues space. Here, the crystal orientation is represented based on the unique association of a rotation axis, denoted as n, and a counterclockwise angle, represented by θ, about n. A proper axis-angle rotation pair (i.e., θ and n) can relate the sample orientation to the crystallographic orientation. The corresponding Rodrigues parameterization, denoted as r, can be computed as $r = n\tan(\frac{\theta}{2})$. The lattice structure of the material of interest in this paper (i.e., 316L stainless steel) is of cubic symmetry. Such a lattice structure reduces the orientational space to a small subset, called the fundamental region that accounts for the cubic symmetry of the lattice structure in the scanned material. The resulting fundamental Rodrigues region is illustrated in Fig. 8(a). For numerical analysis, the fundamental region can be discretized using a tetrahedral finite-element mesh. However, due to cubic symmetry, several of the nodes in the grid are equivalent. Hence, the fundamental region can be further reduced to a smaller set of independent nodes colored in blue as shown in Fig. 8(b). Accordingly, each point in the EBSD dataset is mapped to the closest independent node in the discretized ODF space. The measured EBSD images are then colored according to the nodal numbers. A simple choice for the colormap, as depicted in Fig. 8(c), is to apply the Rodrigues vector itself for each independent node as an RGB triplet. Subsequently, for MRF reconstruction, a subset of experimental EBSD sections of size 256×256 μm^2 along each orthogonal axis is then selected and re-sampled to 128×128 pixels. Note, the reconstruction scheme presented in this work is not tied to a specific input resolution. Thus, any 2D image resolution can be reconstructed, if needed. The implication is that the user should ensure to specify a sufficient pixel resolution to capture the phenomena of interest. Following this, the texture colorings corresponding to *TD* and *SD* directions were adjusted such that they represent a similar histogram as of *BD* image. The additive manufacturing processes tend to create large variations in the crystallographic texture across a specimen. As such, performing *histogram matching* can establish a consistent texture in the volumetric MRF unit cell, as images are taken at different locations within the specimen. Fig. 9(a) elucidates the orthogonal set of images for 316L stainless steel specimen as inputted to the MRF reconstruction algorithm. The 3D EBSD image from the MRF algorithm is shown in Fig. 9(b). A number of different sections of the reconstructed model across *TD* axis are also shown in
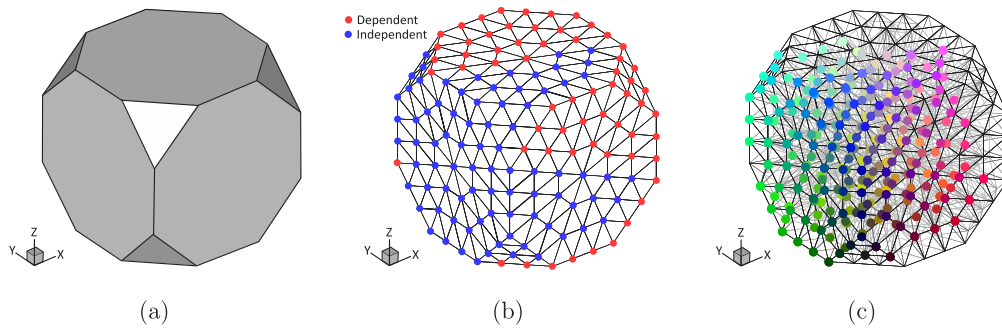
Fig. 8. Illustration of Orientation Distribution Function (ODF): (a) the Rodrigues fundamental region for cubic symmetry, (b) a discretized ODF with independent nodes along the external surface, colored blue, (c) applied colormap showing the RGB values of independent nodes in the fundamental region. Here, the internal elements have been faded for a better visualization of the colormap. (For interpretation of the references to color in this figure legend, the reader is referred to the web version of this article.)
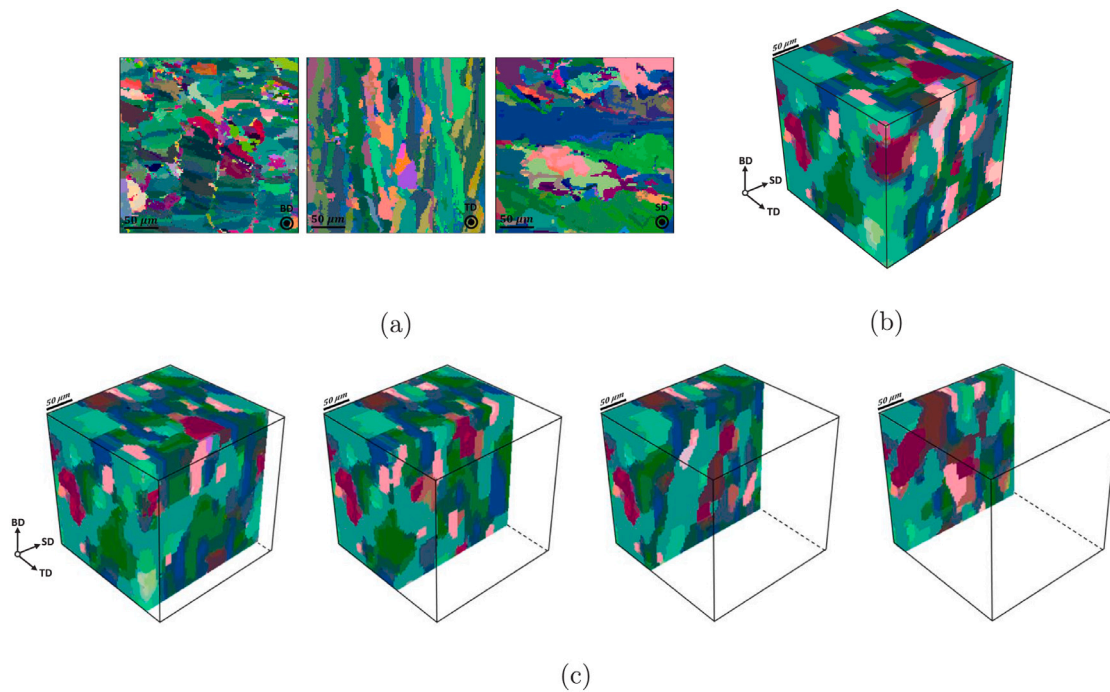
Fig. 9. Illustration of 2D/3D images: (a) set of orthogonal experimental EBSD images of AM 316L stainless steel microstructure as inputted in MRF sampling algorithm, (b) representative 3D MRF reconstructed model, and (c) numerous sectional images of the reconstructed model along *TD* axis.

Fig. 9(c). The averaging step performed in Eq. (2) tends to smoothen the noises within the MRF synthetic model, hence providing an overall smoother reconstruction compared to input 2D exemplars.

Following the reconstruction of the MRF unit cell, each color level of the synthesized model is mapped to an independent node in the fundamental Rodrigues region using the colormap shown in Fig. 8(c). For every voxel in the unit cell, the four closest colors (in Euclidean norm sense) in the discretized ODF space are identified. The voxel coloring remains unaltered, provided the sampled RGB triplet is within the specified threshold. Otherwise, the RGB coloring of the voxel is replaced randomly with one of the four closest independent nodes in the ODF fundamental region. As depicted in Fig. 10(a)–(b), it is found that the resulting pole figures of the MRF reconstructed microstructure closely resemble the measured texture distribution. Such an assessment exhibits the ability of the MRF unit cell reconstruction algorithm to accurately simulate textural descriptions of AM microstructures.

Once the RGB triplets are mapped through the discretized ODF colormap, the grain boundary misorientation angles can be conveniently calculated. In the scheme of grain boundary geometry, the misorientation is defined in terms of the required angle ϕ to bring the two neighboring grains into coincidence about an axis common to
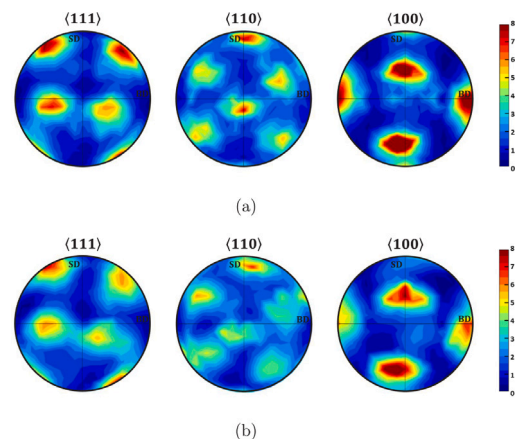

Fig. 10. Texture comparison of $\langle 111 \rangle$, $\langle 110 \rangle$, and $\langle 100 \rangle$ pole figures for: (a) the orthogonal experimental images, against (b) the synthesized 3D MRF microstructure.
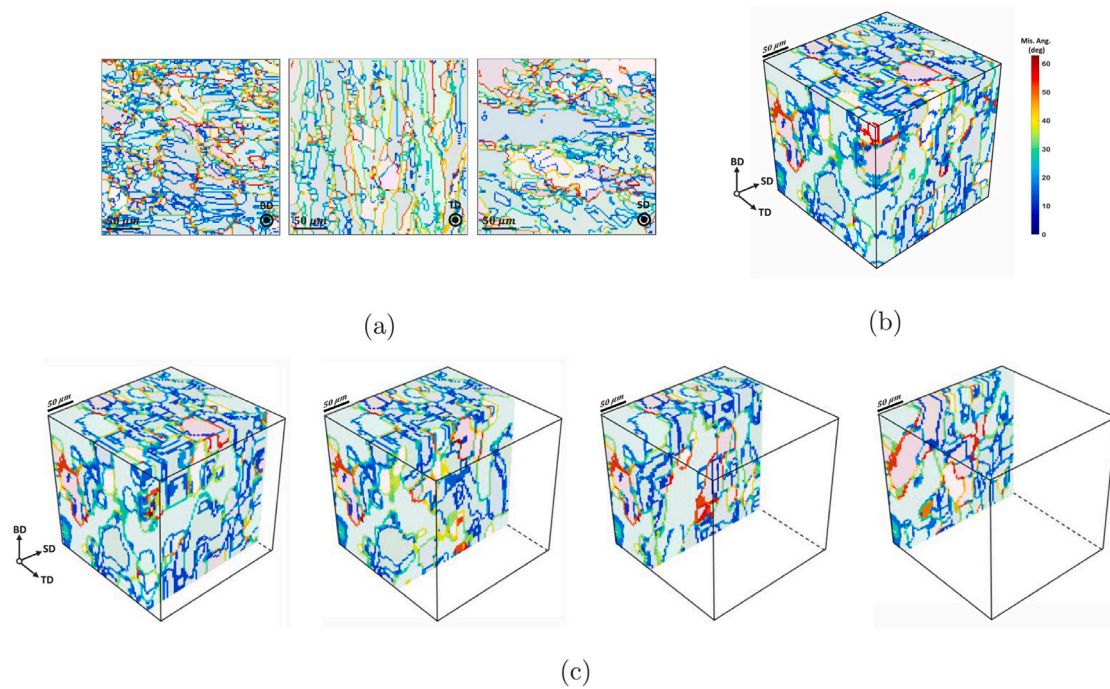
Fig. 11. Illustration of 2D/3D spatial distribution of grain boundary misorientation angles for: (a) set of orthogonal experimental images of 316L stainless steel AM microstructure, (b) representative 3D MRF reconstructed model, and (c) numerous sectional images of the MRF reconstructed model along *TD* axis.

both lattices. Such parameterization is concisely known as the angle-axis misorientation pair. To perform mathematical manipulations, the misorientation is conveniently expressed as a 3×3 orthonormal misorientation matrix $\boldsymbol{M}$. Consequently, for two interfacing grains denoted as grains A and B, the columns of the matrix $\boldsymbol{M}$ are equivalently the direction cosines corresponding to the rotation of the crystal coordinate systems of grain B to grain A, as grain A being the reference grain. The misorientation angle is obtained from the matrix $\boldsymbol{M}$ as follows:

$$2\cos\phi + 1 = \text{tr}(\boldsymbol{M}) \tag{8}$$

where $\text{tr}(\cdot)$ is defined to be the trace or the sum of elements on the main diagonal for an input matrix.

Furthermore, due to the symmetric nature of the crystallography involved, the axes of grain B can be chosen in more than one way in respect to the reference grain A. For cubic symmetry, this multiplicity is precisely 24; that is, there are 24 unique (but equivalent) ways in which the misorientation matrix $\boldsymbol{M}$ can be expressed. This results in 24 angle-axis pairs. Although these angle-axis pairs are all equivalent, it is conventional to report the lowest angle solution when describing a misorientation angle. Accordingly, Low-Angle Grain Boundaries (LAGBs), defined as $\phi < 15°$, are often immediately obvious.

For assessment of grain boundary misorientation angles of the MRF reconstruction, the reconstructed 3D image is properly segmented first. The misorientation angles are then computed slice-by-slice using eight-fold connectivity, where the crystal orientation (i.e., Rodrigues vectors) of every voxel is being compared against its adjacent neighbors (along the horizontal, vertical, and diagonal directions) positioned on each cross-section. If the frequency of the most repeating orientation index in the 3×3 window is within a specified threshold, the two most frequent Rodrigues vectors inside the sampling window are identified. Following this, the misorientation angle between the two most frequently-occurring orientation indices is computed. The same process follows for the orthogonal experimental images. Fig. 11(a)–(b) illustrates the spatial distribution of grain boundary misorientation angles for experimental and 3D synthesized EBSD images, respectively. As expected, the low-angle boundaries ranging between $0° - 15°$, as illustrated in Fig. 11, are highly pronounced in both sets of images.

The corresponding spatial distribution of misorientation angles of the sections in Fig. 9(c) are also depicted in Fig. 11(c). Thereafter, the High-Angle Grain Boundary (HAGB) misorientation values (referred to as misorientation angles greater or equal to 15°) are sorted to allow for a quantitative comparison between experimental and synthesized images. The probability densities of the HAGBs for the set of three orthogonal images and cross-sections of the reconstructed MRF model, as seen in Fig. 12 are then calculated over 21 bins. Here, because of the cubic symmetry of the measured specimen's lattice structure, the maximum unique misorientation angle possible is limited to 62.8°. Overall, a close agreement between the scanned and reconstructed MRF images is observed, with the 3D reconstruction predicts marginally a lower probability for misorientation angles ranging between $40° - 52°$.
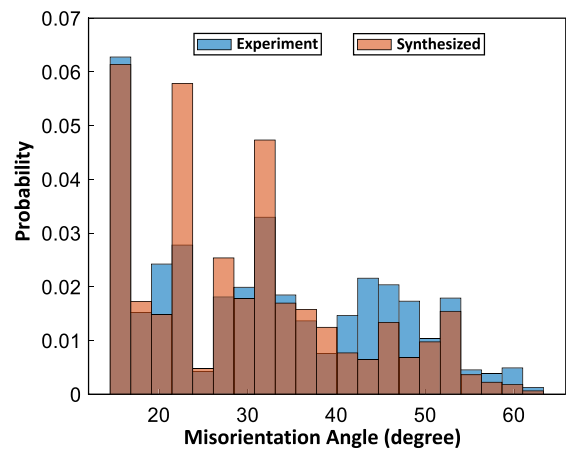

Fig. 12. Comparison of PDF of HAGB misorientation angles of the 3D synthesized MRF microstructure against experimental imaging. Here, the probability densities of the misorientation angles are computed over 21 bins. The maximum unique misorientation angle possible due to cubic symmetry is 62.8°.

Next, the ability of the MRF algorithm to accurately model grain size statistics of the 316L stainless steel microstructure along *TD* axis as compared to the respective input experimental exemplar is examined.
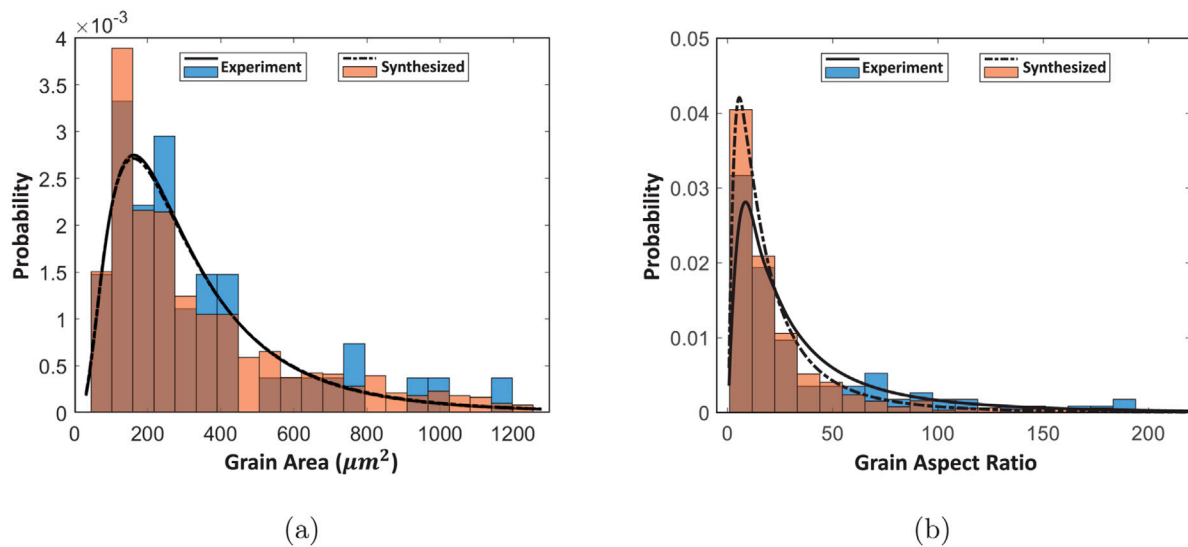
Fig. 13. Comparison of PDFs for (a) grain size, and (b) aspect ratio of the 3D synthesized microstructure against experimental imaging along *TD* axis. The probability densities of the measured statistics are computed over 21 bins and fitted using a log-normal distribution.

Grain size distribution is essential for simulating mechanical properties in AM structures using Hall–Petch models [59,60]. In this assessment, grain sizes of the 2D EBSD image are obtained using the following procedure. The incomplete grains along the outer edges adjacent to the borders of the experimental EBSD image are removed. For every inner crystal, the grain areas, along with the ratio of the major over minor diameters of the best-fitting ellipse with an equivalent normalized second central moments, are computed and stored. Afterward, abnormally small and large grains are removed from the measured grain area dataset. The histograms of the grain area and the corresponding aspect ratio for each grain, as depicted in Figs. 13(a)–(b) respectively, are then plotted over 21 bins using a log-normal fit. Similarly, to capture the grain size distribution of the 3D synthesized unit cell, slices along the *TD* axis are extracted, and the same process as used in the 2D exemplar is applied. That is, the external grains for every slice are first eliminated, and for each inner grain, the grain area and its respective aspect ratio are obtained. Here, aspect ratios near one represent near-circular (i.e., equiaxed) grain morphology. In contrast, values close to ∞ represent needle-like cross-sections. When comparing grain size statistics, both the simulated and experimental log-normal distributions peak near 160 μm^2, indicating a considerable fraction of small-size grains in the dataset. Additionally, on the *TD* plane, nearly 51.9% and 47.6% of the grains in experimental and simulated images, respectively, have aspect ratios ranging from 5 to 20. This implies that a large fraction of the realized 316L stainless steel microstructure on *TD* surface consists of highly-elongated morphologies, which is also evident in Fig. 9. Overall, as illustrated in Fig. 13, close agreements between the input experimental image and MRF reconstruction are observed, with minor deviations seen for the low-frequency components, where the 3D MRF reconstruction marginally predicts a lower probability.

Thereafter, the LEGOMAT reconstruction technique follows by constructing global models shown in Fig. 14, based on the single locally-extracted MRF microstructure shown in Fig. 9(b). The LEGOMAT approach presented in this paper is not tied to the MRF numerical reconstruction algorithm only and can be coupled with a wide variety of unit cell microstructural exemplars obtained from other computational frameworks (e.g., Voronoi tessellation [17], DREAM.3D [46], Neper [45], supervised learning [28], etc.) or even experimental 3D images [23,26,27]. The MRF reconstruction algorithm, however, is specifically advantageous for building realistic small-scale AM unit cells from a single set of orthogonal 2D planar exemplars. The LEGOMAT numerical approach is to embed the reconstructed 3D microstructures in the CAD geometry based on experimentally observed insights on

AM microstructure formation, as it is inherently controlled by solidification rate and thermal gradient, which are also functions of laser parameters (e.g., speed, power) and the laser path (e.g., hatch spacing, layer thickness). The effects of cooling rate and temperature gradient history on microstructural patterns during the solidification process have been well studied in literature [35,50,51,57]. Key components seen in the solidification process include: (*i*) smaller grain growth near the laser track because of the high-temperature profile at the solid–liquid interface, (*ii*) elongated grains away from the laser spot in-plane to the surface of the build, and (*iii*) on *SD* face, the elongated grains tend to grow perpendicular to the melt pool's solidification surface, bending toward the laser track [61,62]. The resulting heterogeneous mixture of elongated and equiaxed grains often has a visible periodicity with the deposition thickness, hatch spacing, and scanning pattern.

The preferred crystallographic growth direction is often specified primarily by the heat flow direction. The grain size scaling of a build, on the other hand often decreases with increasing laser speed or decreasing laser power [58]. As a result of such geometrical principles, a natural way to describe grain formation during the solidification process is to align microstructural unit cells in the 3D geometrical space using a material flow field as shown in Fig. 14(left). Generally, these user-drawn vector fields work best when they are divergence-free, as artifacts can appear around material flow fields with singularities (e.g., sink or source points). The issue of microstructural artifacts with singular vector fields can often be alleviated to some extent by locally enhancing the mesh density (subdividing the tetrahedral elements) at such regions, or equivalently by reducing the grain size scaling, prior to LEGOMAT optimization procedure. In addition to the material flow fields, the grain size scaling is represented using the same approach as described in Section 2.2.2, with smaller grains along the laser path gradually transitioning to columnar grains near the melt pool's boundary. Such geometric reconstruction methodology can systematically simulate the preferred grain growth directionality and size scaling for large-scale engineering components manufactured by laser additive manufacturing processes consisting of several passes and deposition layers. Fig. 14(right) presents the final reconstructed outputs, displaying the grain sizes and shapes that result from the LEGOMAT optimization procedure for various simulations, ranging from a single-layer to multi-layer multi-track scenarios. This method can readily extend to simulate dozens of deposition layers and hundreds of laser passes. The CAD models for the block geometries illustrated in Figs. 14(a)–(c) contain 22992, 31424, and 51312 linear tetrahedral elements, respectively. Once generated, these synthetic large-scale AM
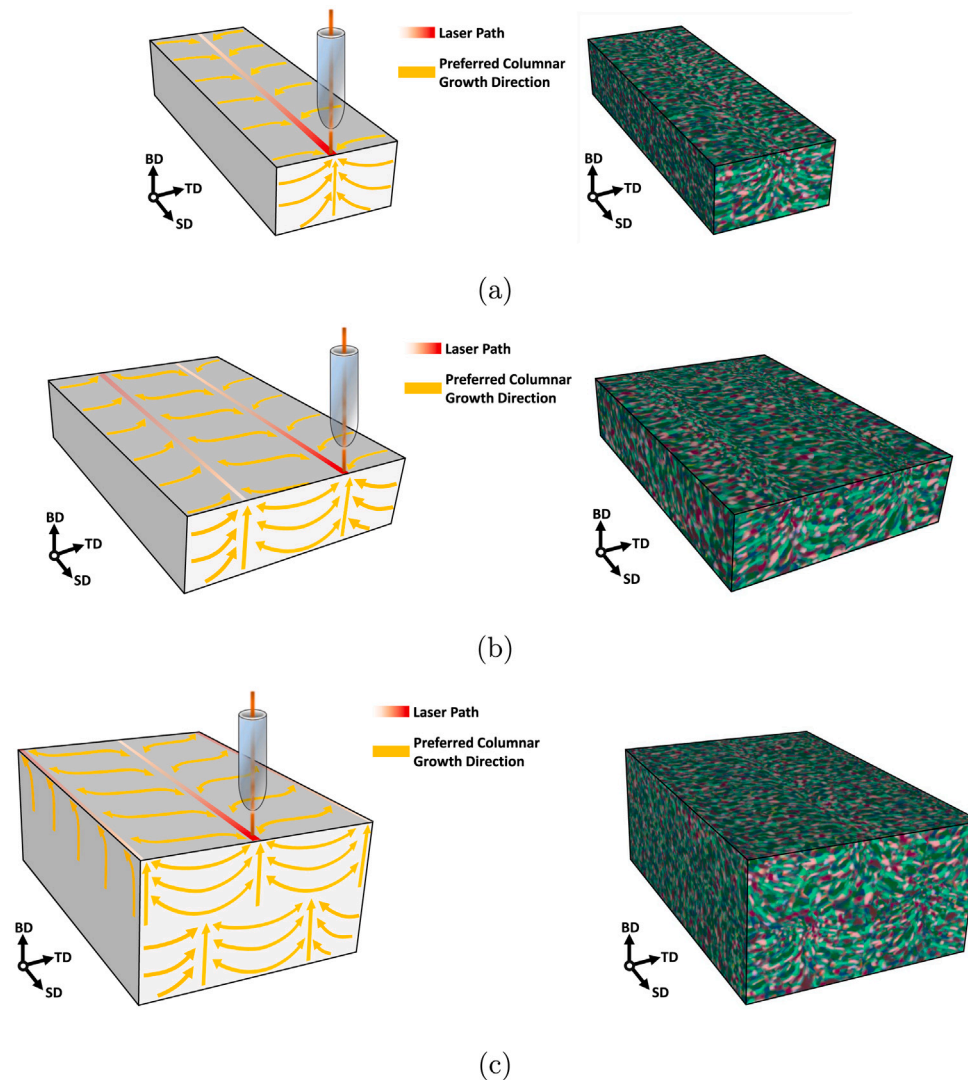
Fig. 14. Illustration of LEGOMAT embedding algorithm for simulating AM microstructures for (a) a single-track single-layer example, (b) a double laser-track across a single-layer CAD model, and (c) a double-layer simulation with a zig-zag scanning pattern. Here, the laser paths and vector fields representing the preferred columnar growth direction for each case are shown on the left. Upon embedding microstructural patches, smaller grain sizes are pasted along the laser path and are quickly transforming to columnar grains away from the laser beam track.

microstructures can be used in various material performance simulations (e.g., material mechanics, conductivity, etc.) [17,18,63,64] or otherwise provide insights for multi-dimensional analysis involving desirable processing modalities and performance metrics [38], which is an extremely difficult task to achieve by experimental means alone.

To further demonstrate the flexibility of the presented LEGOMAT strategy, an assessment of the LEGOMAT simulated microstructure against SPPARKS kinetic Monte Carlo simulation [32] with respective experimental EBSD images is provided. The build in this example is deposited using the LENS technique with a defocused high-power laser beam, rastering back and forth at a rate of 10.58 mm/s, with intended layer thickness and hatch spacing of 1.25 mm and 2 mm, respectively. Such a processing pattern results in similar formation principle as outlined in Sections 2.2.1–2.2.2. In short, curved columnar grains are formed on *TD* and *SD* planes, and on the *BD* plane, large grains elongate across the central regions while transitioning to finer grains along each laser track [65]. These grain types are illustrated in Fig. 15 alongside three orthogonal cross-sections of the build. The illustrated *TD* images in Fig. 15 are taken from the centerline of the beam pass. Qualitatively on *BD* plane, both simulated microstructures correctly alternate between fine grains at the center to larger transversely-elongated structures. Additionally, in the *SD* plane, vertically-oriented

grains found at the center of each pass transition to exceptionally curved grains in between. The grains along the *TD* plane illustrate vertically-elongated grains slightly incline toward the *SD* at the top. The strength of the LEGOMAT approach, as presented in this example, is its ability to efficiently create 3D microstructures with spatially-varying highly-curved non-convex structures over large regions at significantly lower computational cost than existing large-scale texture synthesis algorithms applicable for additive manufacturing. Additionally, as depicted in Fig. 15, physics-based models such as the kinetic Monte Carlo simulator often have difficulty modeling the textural descriptions (e.g., grain size and curvature) of AM specimens. As a result, the LEGOMAT algorithm offers an alternative solution for the rapid visualization of microstructural variations with diverse processing parameters. This is exceedingly important as AM microstructures vary both globally with machine inputs and locally with build geometry, hence making experimental characterization of AM build seemingly impossible.

Additionally, since experimental information along all three orthogonal directions is available, quantitative comparisons of the experimental and simulated results are possible. Fig. 16 displays histograms of grain size statistics for both SPPARKS (on top) and LEGOMAT (on bottom) against the experimental microstructures across the three orthogonal planes illustrated in Fig. 15. To obtain the grain size statistics,
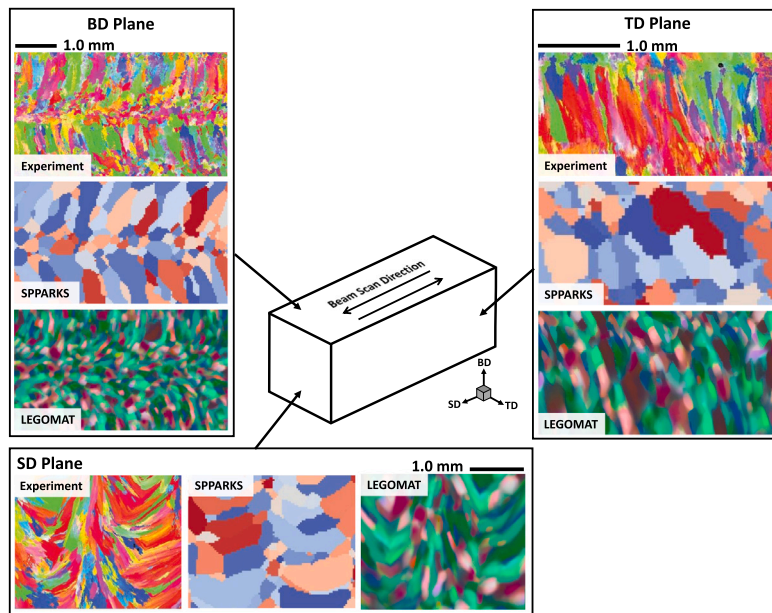
Fig. 15. Comparison between experimental and simulated AM microstructures using SPPARKS kinetic Monte Carlo simulator and LEGOMAT geometrical approach along orthogonal planes. The experimental and SPPARKS simulated images shown here are reproduced from the work of Rodgers et al. [32] under the terms of the Creative Commons CC-BY license.

a similar procedure as in Fig. 13 is applied. That is, all images are first segmented, and boundary grains along the border are removed. The grain areas of all inner grains, excluding abnormally small and large grains, are obtained, and subsequently plotted using a log-normal fit. Across each orthogonal plane, the LEGOMAT's log-normal distribution is found to be closely following the experimental distribution. This is while SPPARKS simulated results are shown to deviate significantly for smaller-scale grain sizes.

The simulated results presented for the LEGOMAT reconstruction framework show significant promise for the generation of large-scale AM microstructures. However, the manual drawing of the volumetric

vector field can be relatively time-consuming, especially for multi-layer, multi-track examples. For instance, it takes the user about 18 minutes to create a direction field for the CAD model shown in Fig. 14(c), whereas the scaling parameterization of the patches takes about 8 minutes, and only 7 minutes to finalize the numerical computation pertaining to LEGOMAT embedding process using a PC with 3.0 GHz CPU and 64.0 GB RAM. Consequently, future work will focus on automating the manual drawing of the preferred direction field as well as the parameterization of grain scaling based on a set of user-defined processing parameters (e.g., hatch spacing, layer thicknesses, scanning pattern, etc.). Nonetheless, the LEGOMAT methodology presented in this paper
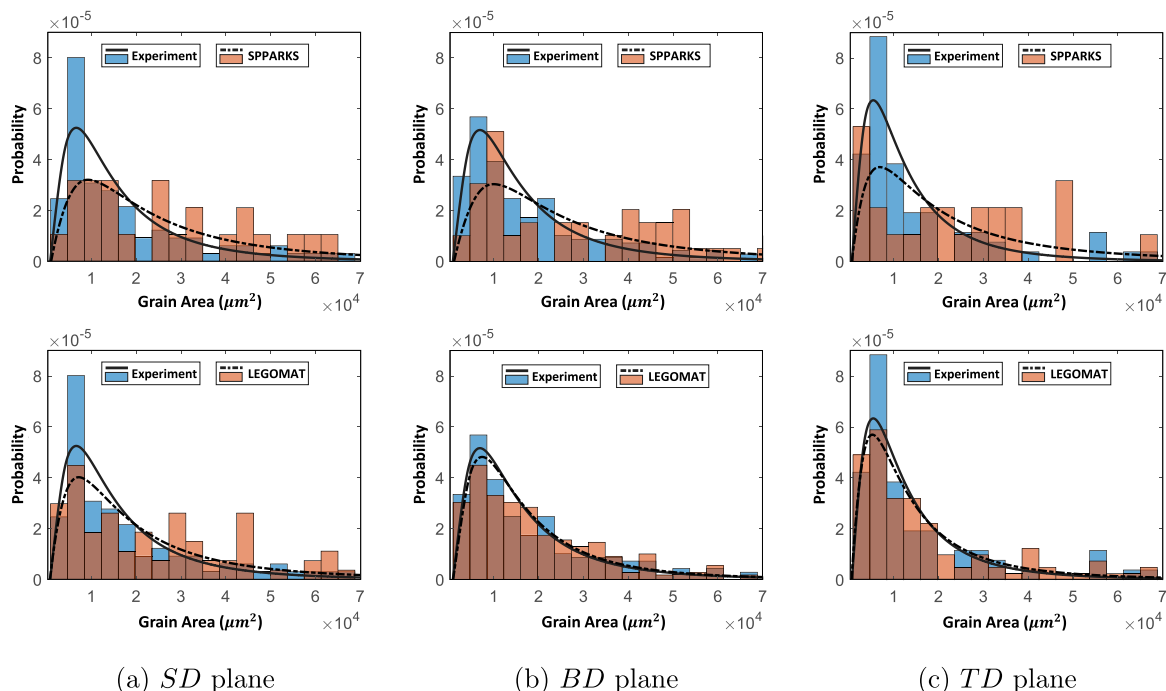

(a) SD plane   (b) BD plane   (c) TD plane

Fig. 16. Comparison of grain size statistics for simulated SPPARKS kinetic Monte Carlo [32] (on top) and LEGOMAT (on bottom) microstructures against experimental images across orthogonal (a) SD, (b) BD, and (c) TD planes.

is still significantly computationally inexpensive compared to existing physics-based models [30–32,34,35] for representing large-scale AM solid textures.

Furthermore, the current LEGOMAT reconstruction framework is limited to embedding a single 3D microstructural snapshot in the CAD model. However, the LEGOMAT approach can benefit from multiple input 3D exemplars imaged across various spatial locations. One approach for direct implementation of spatial variations of the AM microstructure is to exploit the mean locations of the input microstructural measurements in order to partition the CAD geometry in the form of a Voronoi diagram. Mathematically, the measured locations directly correspond to the centroid of the convex hull within each partition, which is also correlated with differences in microstructural features (e.g., grain size, shape, etc.). Accordingly, the Voronoi diagram can provide a geometrical partitioning of the CAD specimen, where the best-matching measured 3D unit cell can be identified (based on its relative spatial coordinates to the laser path) and then be sampled for the patching/embedding process. Additionally, a numerical method can be developed to progressively enhance the resultant embedding process based/conditioned on available input datasets. Here, geometric partitioning of the CAD specimen can be updated as new measured 3D microstructures become available. In this approach, regions in the CAD model for which new reclassifications are available will be partitioned and then progressively re-sampled/re-patched. Work on this is still in progress and will be reported in future articles.

4. Conclusions

In this paper, an image-based framework is introduced for 3D microstructure synthesis of metal AM materials over very large length-scale CAD models. The complete workflow from orthogonal 2D experimental EBSD images to a full-field microstructural CAD visualization is an important and novel contribution in this work. Here, a set of three EBSD exemplars imaged on orthogonal planes of a 316L stainless steel specimen manufactured by SLM process is first obtained via SEM acquisition technique. The microstructures are subsequently converted to a 3D representative unit cell using the MRF sampling technique. The MRF algorithm reconstructs 3D images through matching orthogonal neighborhoods of each voxel to the sectional experimental micrographs, while ensuring that the sampled voxels taken from the 2D input exemplars have meshed together seamlessly in the 3D synthesized image. Thereafter, statistical analyses of microstructural features, such as grain size, orientation distribution, and grain boundary misorientation angles for the reconstructed 3D microstructures, are carried out against the original 2D EBSD images. The results demonstrate that MRF can effectively predict both textural and morphological descriptions of AM microstructures at a small-length scale.

The variations of 3D microstructures during a laser additive manufacturing process at larger length-scales are then captured using the LEGOMAT tensor-based optimization process. The LEGOMAT optimization procedure embeds 3D microstructures in a part-scale CAD geometry accordant with the user-specified material flow fields that efficiently incorporate microstructural variations (e.g., grain size, shape, curvature, anisotropy, and growth direction) in structural systems consisting of several laser paths and deposition layers. Such formulation is shown to be highly effective for modeling the location-specific microstructural geometries seen in experimental characterization techniques. For instance, across *BD* surface, fine-size equiaxed grains often nucleate near the laser track and then quickly transition to larger transversely-elongated grains in between the laser paths. Similarly, on the *TD* plane near the laser beam track, elongated grains tend to incline toward the *SD*. On the *SD* plane, the columnar grains tend to grow perpendicular to the melt pool's solidification surface, curving toward the laser beam direction. As a result, the LEGOMAT approach can provide in real-time, an efficient methodology to describe textural components in 3D geometrical CAD space via a user-defined tensor field, capturing the

preferred growth directions during the solidification process. Due to the large-scale microstructure reconstruction model being primarily based on geometrical principles, the LEGOMAT methodology is extremely robust and requires minimal computational power and memory, compared to existing AM microstructure simulation techniques. Near-term future work will focus on (*i*) implementing an encoder that accepts a number of input microstructural unit cells while down selects the best 3D exemplar during each embedding iteration based on the relative spatial location of the microstructural patch within the CAD model to its nearest laser path, and (*ii*) automating the manual specifications of the preferred growth orientation and grain size parameterization.

CRediT authorship contribution statement

Iman Javaheri: Conceptualization, Methodology, Software, Visualization, Validation, Formal analysis, Investigation, Writing – original draft, Writing – review & editing, Funding acquisition. **Mohsen Taheri Andani:** Experiments, Investigation, Writing – review & editing. **Veera Sundararaghavan:** Conceptualization, Methodology, Software, Supervision, Project administration, Writing – original draft, Funding acquisition.

Declaration of competing interest

The authors declare that they have no known competing financial interests or personal relationships that could have appeared to influence the work reported in this paper.

Data availability

The executable and data files for the methodology described in this paper are available upon reasonable request.

Acknowledgments

References

[1] M. Sangid, J.F. Matlik, A. Keskin, B.H. Thacker, B.J. Bichon, D.L. Ball, S.P. Engelstad, C. Ward, V. Venkatesh, H.A. Kim, et al., Integrating ICME practices into design systems and structural analysis, in: 55th AIAA Aerospace Sciences Meeting, 2017, p. 0874.

[2] W. Xu, E.W. Lui, A. Pateras, M. Qian, M. Brandt, In situ tailoring microstructure in additively manufactured Ti-6Al-4V for superior mechanical performance, Acta Mater. 125 (2017) 390–400.

[3] P. Köhnen, M. Létang, M. Voshage, J.H. Schleifenbaum, C. Haase, Understanding the process-microstructure correlations for tailoring the mechanical properties of L-PBF produced austenitic advanced high strength steel, Addit. Manuf. 30 (2019) 100914.

[4] C. Körner, H. Helmer, A. Bauereiß, R.F. Singer, Tailoring the grain structure of IN718 during selective electron beam melting, in: MATEC Web of Conferences, 14, EDP Sciences, 2014, 08001.

[5] T. Kurzynowski, K. Gruber, W. Stopyra, B. Kuźnicka, E. Chlebus, Correlation between process parameters, microstructure and properties of 316L stainless steel processed by selective laser melting, Mater. Sci. Eng. A 718 (2018) 64–73.

[6] N. Raghavan, R. Dehoff, S. Pannala, S. Simunovic, M. Kirka, J. Turner, N. Carlson, S.S. Babu, Numerical modeling of heat-transfer and the influence of process parameters on tailoring the grain morphology of IN718 in electron beam additive manufacturing, Acta Mater. 112 (2016) 303–314.

[7] T. Gatsos, K.A. Elsayed, Y. Zhai, D.A. Lados, Review on computational modeling of process–microstructure–property relationships in metal additive manufacturing, JOM 72 (1) (2020) 403–419.

[8] W. Yan, S. Lin, O.L. Kafka, Y. Lian, C. Yu, Z. Liu, J. Yan, S. Wolff, H. Wu, E. Ndip-Agbor, et al., Data-driven multi-scale multi-physics models to derive process–structure–property relationships for additive manufacturing, Comput. Mech. 61 (5) (2018) 521–541.

[9] P.I. O'Toole, M.J. Patel, C. Tang, D. Gunasegaram, A.B. Murphy, I.S. Cole, Multiscale simulation of rapid solidification of an aluminium-silicon alloy under additive manufacturing conditions, Addit. Manuf. 48, Part A (2021) 102353.

[10] B.B. He, Introduction to two-dimensional X-ray diffraction, Powder Diffr. 18 (2) (2003) 71–85.

[11] P. Krakhmalev, G. Fredriksson, K. Svensson, I. Yadroitsev, I. Yadroitsava, M. Thuvander, R. Peng, Microstructure, solidification texture, and thermal stability of 316L stainless steel manufactured by laser powder bed fusion, Metals 8 (8) (2018) 643.

[12] Q. Zhang, J. Chen, P. Guo, H. Tan, X. Lin, W. Huang, Texture and microstructure characterization in laser additive manufactured Ti–6Al–2Zr–2Sn–3Mo–1.5 Cr–2Nb titanium alloy, Mater. Des. 88 (2015) 550–557.

[13] H. Qin, V. Fallah, Q. Dong, M. Brochu, M.R. Daymond, M. Gallerneault, Solidification pattern, microstructure and texture development in laser powder bed fusion (LPBF) of Al10SiMg alloy, Mater. Charact. 145 (2018) 29–38.

[14] M.A. Groeber, B. Haley, M.D. Uchic, D.M. Dimiduk, S. Ghosh, 3D reconstruction and characterization of polycrystalline microstructures using a FIB–SEM system, Mater. Charact. 57 (4–5) (2006) 259–273.

[15] R. DeHoff, Quantitative serial sectioning analysis: Preview, J. Microsc. 131 (3) (1983) 259–263.

[16] D. Deng, R.L. Peng, H. Brodin, J. Moverare, Microstructure and mechanical properties of Inconel 718 produced by selective laser melting: Sample orientation dependence and effects of post heat treatments, Mater. Sci. Eng. A 713 (2018) 294–306.

[17] S. Ganesan, I. Javaheri, V. Sundararaghavan, Constrained Voronoi models for interpreting surface microstructural measurements, Mech. Mater. 159 (2021) 103892.

[18] A. Lakshmanan, J. Luo, I. Javaheri, V. Sundararaghavan, Three-dimensional crystal plasticity simulations using peridynamics theory and experimental comparison, Int. J. Plast. 142 (2021) 102991.

[19] G.E. Ice, B.C. Larson, Three-dimensional X-ray structural microscopy using polychromatic microbeams, MRS Bull. 29 (3) (2004) 170–176.

[20] M. Groeber, S. Ghosh, M.D. Uchic, D.M. Dimiduk, A framework for automated analysis and simulation of 3D polycrystalline microstructures.: Part 1: Statistical characterization, Acta Mater. 56 (6) (2008) 1257–1273.

[21] D. Rowenhorst, A. Gupta, C. Feng, G. Spanos, 3D crystallographic and morphological analysis of coarse martensite: Combining EBSD and serial sectioning, Scr. Mater. 55 (1) (2006) 11–16.

[22] J.E. Spowart, Automated serial sectioning for 3-D analysis of microstructures, Scr. Mater. 55 (1) (2006) 5–10.

[23] D.J. Rowenhorst, L. Nguyen, A.D. Murphy-Leonard, R.W. Fonda, Characterization of microstructure in additively manufactured 316L using automated serial sectioning, Curr. Opin. Solid State Mater. Sci. 24 (3) (2020) 100819.

[24] H.F. Poulsen, D.J. Jensen, G.B. Vaughan, Three-dimensional X-ray diffraction microscopy using high-energy X-rays, MRS Bull. 29 (3) (2004) 166–169.

[25] J.-Y. Buffiere, E. Ferrie, H. Proudhon, W. Ludwig, Three-dimensional visualisation of fatigue cracks in metals using high resolution synchrotron X-ray micro-tomography, Mater. Sci. Technol. 22 (9) (2006) 1019–1024.

[26] E. Maire, P.J. Withers, Quantitative X-ray tomography, Int. Mater. Rev. 59 (1) (2014) 1–43.

[27] S. McDonald, P. Reischig, C. Holzner, E. Lauridsen, P. Withers, A. Merkle, M. Feser, Non-destructive mapping of grain orientations in 3D by laboratory X-ray microscopy, Sci. Rep. 5 (2015) 14665.

[28] R. Bostanabad, W. Chen, D. Apley, Characterization and reconstruction of 3D stochastic microstructures via supervised learning, J. Microsc. 264 (3) (2016) 282–297.

[29] R. Bostanabad, A.T. Bui, W. Xie, D.W. Apley, W. Chen, Stochastic microstructure characterization and reconstruction via supervised learning, Acta Mater. 103 (2016) 89–102.

[30] T. Keller, G. Lindwall, S. Ghosh, L. Ma, B.M. Lane, F. Zhang, U.R. Kattner, E.A. Lass, J.C. Heigel, Y. Idell, et al., Application of finite element, phase-field, and CALPHAD-based methods to additive manufacturing of Ni-based superalloys, Acta Mater. 139 (2017) 244–253.

[31] S. Ghosh, L. Ma, N. Ofori -Opoku, J.E. Guyer, On the primary spacing and microsegregation of cellular dendrites in laser deposited Ni–Nb alloys, Modelling Simul. Mater. Sci. Eng. 25 (6) (2017) 065002.

[32] T.M. Rodgers, J.D. Madison, V. Tikare, Simulation of metal additive manufacturing microstructures using kinetic Monte Carlo, Comput. Mater. Sci. 135 (2017) 78–89.

[33] T.M. Rodgers, D. Moser, F. Abdeljawad, O.D.U. Jackson, J.D. Carroll, B.H. Jared, D.S. Bolintineanu, J.A. Mitchell, J.D. Madison, Simulation of powder bed metal additive manufacturing microstructures with coupled finite difference-Monte Carlo method, Addit. Manuf. 41 (2021) 101953.

[34] A. Zinoviev, O. Zinovieva, V. Ploshikhin, V. Romanova, R. Balokhonov, Evolution of grain structure during laser additive manufacturing. simulation by a cellular automata method, Mater. Des. 106 (2016) 321–329.

[35] A.R.A. Dezfoli, W.-S. Hwang, W.-C. Huang, T.-W. Tsai, Determination and controlling of grain structure of metals after laser incidence: Theoretical approach, Sci. Rep. 7 (2017) 41527.

[36] E. Miyoshi, T. Takaki, M. Ohno, Y. Shibuta, S. Sakane, T. Aoki, Large-scale phase-field simulation of three-dimensional isotropic grain growth in polycrystalline thin films, Modelling Simul. Mater. Sci. Eng. 27 (5) (2019) 054003.

[37] J.A. Koepf, M.R. Gotterbarm, M. Markl, C. Körner, 3D multi-layer grain structure simulation of powder bed fusion additive manufacturing, Acta Mater. 152 (2018) 119–126.

[38] E. Popova, T.M. Rodgers, X. Gong, A. Cecen, J.D. Madison, S.R. Kalidindi, Process-structure linkages using a data science approach: Application to simulated additive manufacturing data, Integr. Mater. Manuf. Innov. 6 (1) (2017) 54–68.

[39] R. Bostanabad, Reconstruction of 3D microstructures from 2D images via transfer learning, Comput. Aided Des. 128 (2020) 102906.

[40] P. Acar, V. Sundararaghavan, A Markov random field approach for modeling spatio-temporal evolution of microstructures, Modelling Simul. Mater. Sci. Eng. 24 (7) (2016) 075005.

[41] A. Senthilnathan, P. Acar, M. De Graef, Markov random field based microstructure reconstruction using the principal image moments, Mater. Charact. 178 (2021) 111281.

[42] V. Sundararaghavan, Reconstruction of three-dimensional anisotropic microstructures from two-dimensional micrographs imaged on orthogonal planes, Integr. Mater. Manuf. Innov. 3 (1) (2014) 240–250.

[43] I. Javaheri, V. Sundararaghavan, Polycrystalline microstructure reconstruction using Markov random fields and histogram matching, Comput. Aided Des. 120 (2020) 102806.

[44] H. Si, On refinement of constrained Delaunay tetrahedralizations, in: Proceedings of the 15th International Meshing Roundtable, Springer, 2006, pp. 509–528.

[45] R. Quey, L. Renversade, Optimal polyhedral description of 3D polycrystals: Method and application to statistical and synchrotron X-ray diffraction data, Comput. Methods Appl. Mech. Engrg. 330 (2018) 308–333.

[46] M.A. Groeber, M.A. Jackson, DREAM. 3D: A digital representation environment for the analysis of microstructure in 3D, Integr. Mater. Manuf. Innov. 3 (1) (2014) 56–72.

[47] H. Wei, J. Elmer, T. DebRoy, Origin of grain orientation during solidification of an aluminum alloy, Acta Mater. 115 (2016) 123–131.

[48] Y. Balit, E. Charkaluk, A. Constantinescu, Digital image correlation for microstructural analysis of deformation pattern in additively manufactured 316L thin walls, Addit. Manuf. 31 (2020) 100862.

[49] E. Cederberg, V.A. Hosseini, C. Kumara, L. Karlsson, Physical simulation of additively manufactured super duplex stainless steels–microstructure and properties, Addit. Manuf. 34 (2020) 101269.

[50] H. Wei, J. Elmer, T. DebRoy, Crystal growth during keyhole mode laser welding, Acta Mater. 133 (2017) 10–20.

[51] H. Wei, J. Elmer, T. DebRoy, Three-dimensional modeling of grain structure evolution during welding of an aluminum alloy, Acta Mater. 126 (2017) 413–425.

[52] V. Fallah, M. Alimardani, S.F. Corbin, A. Khajepour, Temporal development of melt-pool morphology and clad geometry in laser powder deposition, Comput. Mater. Sci. 50 (7) (2011) 2124–2134.

[53] X. Gong, K. Chou, Phase-field modeling of microstructure evolution in electron beam additive manufacturing, JOM 67 (5) (2015) 1176–1182.

[54] D.A. Field, Laplacian smoothing and Delaunay triangulations, Comm. Appl. Numer. Meth. 4 (6) (1988) 709–712.

[55] K. Takayama, M. Okabe, T. Ijiri, T. Igarashi, Lapped solid textures: Filling a model with anisotropic textures, in: ACM SIGGRAPH 2008 papers, 2008, pp. 1–9.

[56] E. Praun, A. Finkelstein, H. Hoppe, Lapped textures, in: Proceedings of the 27th Annual Conference on Computer Graphics and Interactive Techniques, 2000, pp. 465–470.

[57] A. Badillo, C. Beckermann, Phase-field simulation of the columnar-to-equiaxed transition in alloy solidification, Acta Mater. 54 (8) (2006) 2015–2026.

[58] Č. Donik, J. Kraner, I. Paulin, M. Godec, Influence of the energy density for selective laser melting on the microstructure and mechanical properties of stainless steel, Metals 10 (7) (2020) 919.

[59] S. Sun, V. Sundararaghavan, A probabilistic crystal plasticity model for modeling grain shape effects based on slip geometry, Acta Mater. 60 (13–14) (2012) 5233–5244.

[60] M.T. Andani, A. Lakshmanan, V. Sundararaghavan, J. Allison, A. Misra, Quantitative study of the effect of grain boundary parameters on the slip system level Hall-petch slope for basal slip system in Mg-4Al, Acta Mater. 200 (2020) 148–161.

[61] S. Dryepondt, P. Nandwana, P. Fernandez-Zelaia, F. List III, Microstructure and high temperature tensile properties of 316L fabricated by laser powder-bed fusion, Addit. Manuf. 37 (2021) 101723.

[62] F. Vecchiato, H. de Winton, P. Hooper, M. Wenman, Melt pool microstructure and morphology from single exposures in laser powder bed fusion of 316L stainless steel, Addit. Manuf. 36 (2020) 101401.

[63] M.M. Francois, A. Sun, W.E. King, N.J. Henson, D. Tourret, C.A. Bronkhorst, N.N. Carlson, C.K. Newman, T. Haut, J. Bakosi, et al., Modeling of additive manufacturing processes for metals: Challenges and opportunities, Curr. Opin. Solid State Mater. Sci. 21 (4) (2017) 198–206.

[64] I. Javaheri, J. Luo, A. Lakshmanan, V. Sundararaghavan, Higher-order approximations for stabilizing zero-energy modes in peridynamics crystal plasticity models with large horizon interactions, in: AIAA SciTech 2022 Forum, 2022, p. 0073.

[65] C. Britt, C.J. Montgomery, M.J. Brand, Z.-K. Liu, J.S. Carpenter, A.M. Beese, Effect of processing parameters and strut dimensions on the microstructures and hardness of stainless steel 316L lattice-emulating structures made by powder bed fusion, Addit. Manuf. 40 (2021) 101943.